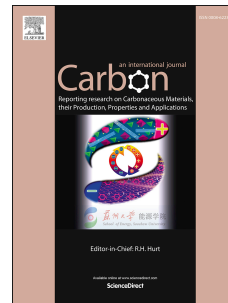# Accepted Manuscript

Low percolation threshold in highly conducting graphene nanoplatelets/glass composite coatings

A. Nistal, E. Garcia, D. Pérez -Coll, C. Prieto, M. Belmonte, M.I. Osendi, P. Miranzo

Please cite this article as: A. Nistal, E. Garcia, D. Pérez -Coll, C. Prieto, M. Belmonte, M.I. Osendi, P. Miranzo, Low percolation threshold in highly conducting graphene nanoplatelets/glass composite coatings, *Carbon* (2018), doi: 10.1016/j.carbon.2018.07.030.

Low percolation threshold in highly conducting graphene nanoplatelets/glass composite coatings

A. Nistal[‡1], E. Garcia[#1], D. Pérez -Coll[1], C. Prieto[2], M. Belmonte[1], M.I. Osendi[1], <u>P. Miranzo</u>[1]*

[1]Institute of Ceramics and Glass (ICV-CSIC), Campus Cantoblanco, C/Kelsen 5, 28049 Madrid, Spain

[2]Instituto de Ciencia de Materiales de Madrid, CSIC, Campus Cantoblanco, 28049 Madrid, Spain

Abstract

Thermal sprayed thick glass coatings with a small percentage of multilayer graphene nanoplatelets (GNP) demonstrate electrical functionality with a quite remarkable low percolation limit (1.18 vol.%). This low critical content and the high electrical conductivity (~ 40 S·m^{-1}) observed for the in-plane direction are related to the peculiar coating microstructure, formed by the pileup of lamellar amorphous particles decorated by GNP mostly following a surface parallel orientation. The general effective media model fitting to the electrical conductivity data for these coatings suggests a 3D connectivity of graphene and estimates an upper limit conductivity for the GNP of 10^5 S·m^{-1}. Hall Effect shows the n-type behavior intrinsic to the SiO_2/graphene interface, and carrier density and mobility rising with the GNP content. In addition, the coatings evidence a very high solar absorptivity that jointly with their high electrical conductivity broadens their potential applications, among others, for electromagnetic interference shielding or as photothermal detector and solar absorber for solar steam generation and water desalination.

Keywords: graphene; hybrid graphene/glass coatings; electrical conductivity; general effective media (GEM); percolation threshold

[#]Present address: School of Mechanical and Aerospace Engineering. Queen's University Belfast, BT9 5AH, UK

[##]Present address: Center for Thermal Spray Research, Stony Brook University, Stony Brook, 11794-2275, NY, USA

*Corresponding author. Tel +(34) 91 7355840 e-mail: pmiranzo@icv.csic.es (Pilar Miranzo)

1. Introduction

During the past decade, graphene-based nanostructures have attracted great attention due to the outstanding mechanical, electrical, thermal and optical properties of graphene [1,2], which have boosted prospective applications in many different fields, such as medicine, membranes, sensors, photonics and (opto)electronics or as multifunctional fillers in paints and composites [3-5]. In the particular case of ceramic composites, both graphene nanoplatelets (GNP) and graphene oxide (GO) have proved their relevant benefits on the mechanical and wear performances for just relatively small additions of these fillers [6], also endowing these composites with additional functionalities such as electrical conduction. In the case of dielectric ceramic matrices such as Si_3N_4, Al_2O_3 or AlN, a typical percolative character is observed with electrical conductivity (σ_m) increments of several orders ($\geq$ 8) of magnitude at volume fractions approaching the percolation limit of the specific nanofiller. In most cases, the simplest percolation model is assumed for predicting the composite behaviour:

$$\sigma_m = \sigma_{h(GNP)} \cdot (V_h - V_{h,c})^t \qquad (1)$$

where, σ_m and $\sigma_{h(GNP)}$ are the conductivities of the composite and the conducting phases, respectively, V_h is the volume fraction of the conducting filler, $V_{h,c}$ is the critical (percolation) volume fraction of the conducting phase, and t is a parameter depending on the connectivity mode. However, differences in the percolation limit ranging between 0.38 and 7.30 vol.% have been reported, critically depending on the average thickness of the graphene nanostructures, i.e. their degree of exfoliation and correspondingly on the processing route used. Accordingly, lower percolation limits are reported for the more easily exfoliated GO sheets, as compared to GNP, having graphene layers firmly attached by Van der Waals forces, and/or when employing colloidal routes [6-10], in contrast to mixing methods where pristine multilayer

graphene is used and, accordingly, graphene exfoliation and restacking become key issues [6, 11]. In this way, it has also been shown that for the same ceramic matrix (Si_3N_4) and processing route (powder blending aided by ultrasonic dispersion in adequate solvents), the electrical conduction threshold diminished in the sequence GNP > GO> graphene nanoribbons (GNR) [8,11,12].

On the other hand, for conducting ceramic matrices, namely SiC, B_4C and ZrB_2, the composites showed comparatively just moderate σ_m increases (3-4 orders of magnitude) with multilayer graphene additions, and what's more, their electrical behaviour was conveniently reproduced by the general rule of mixtures [13].

Besides, graphene-based composites generally show anisotropic electrical conductivity due to the effect of the uniaxial load normally applied during densification that provides a preferential accommodation of GNP perpendicularly to the pressing axis. Consequently, $\sigma_m^{in}/\sigma_m^{cross}$ ratios (*in* and *cross* exponents corresponding to in-plane and cross-plane macro-scale directions, respectively) between 2 and 25 are generally reported [6]. In particular, for the extreme case of a layered composite, consisting in continuous and alternating layers of Si_3N_4 and reduced GO (rGO) paper/film, the effective conductivity was 0.22 S·m^{-1} in the plane parallel to the rGO film; whereas the system was insulator in the perpendicular direction [14].

To the authors' knowledge there is not any study on the electrical percolation of thermal sprayed coatings containing graphene nanofillers despite their very peculiar microstructures. Actually, in a previous work by some of the present authors [15] about the thermal spraying of graphene/glass composite coatings using a composition based on Y_2O_3-Al_2O_3-SiO_2 (YAS) powders and dispersed GNP, a typical lamellar microstructure formed by flattened particles (known as splats) and the GNP expelled to the inter-splat boundaries was evidenced, which was produced by the quenching of

molten particles impinging the substrate. That unique microstructure, hence, induced certain directionality in the thermal conduction and, accordingly, enhanced the damage tolerance of the GNP/YAS coatings. Besides, compared to the blank YAS coating, a superior ablation resistance was demonstrated, which depended on the GNP content and the YAS matrix composition; in particular, on its characteristic temperatures for glass transition, crystallization and melting [16].

We should mention the papers on polymer composite films (~100-200 μm) with graphite fillers [17-20] as previous works reporting low percolation thresholds of conductive coatings/films that also model the effect of the filler orientation on the percolation. Despite the fact that processing conditions, and also properties, of these systems are very different to those of GNP/YAS coatings, the connectivity of the conducting fillers and their percolation behavior present some similarities as will be discuss later.

The present work deeply explores the electrical conduction of the thermal sprayed GNP/YAS glass composite coatings and demonstrates the extremely low percolation threshold achieved due to the GNP network along the inter-splat boundaries. This is the first study on the electrical percolation of graphene/glass composite coatings, analyzing the type of carriers as well and reporting values of the carrier density and mobility on these graphene-based coatings.

2. Experimental

Two different YAS glass matrices were studied, with corresponding compositions located in different zones of the Y_2O_3-Al_2O_3-SiO_2 phase equilibrium diagram and, consequently, showing different temperatures of glass transition, crystallization and

melting, as reflected in Table 1 [21]. These compositions are labeled as YAS-L and YAS-H referring to their low and high melting temperatures, respectively. The justification for using two distinct matrices is based on the search for coatings that with minimal change in composition offer different properties and, accordingly, broaden the scope of their potential applications. Whereas YAS-L is mainly of a glassy nature and easier to process, YAS-H shows certain degree of crystallization and then has a significantly higher temperature resistance [16]. Besides, although the difference in their melting temperatures is only 100 ℃, the energy necessary for melting and reacting the original powders is quite different, in particular about six times higher for YAS-L than for YAS-H, as estimated by differential thermal analysis [16]. This fact strongly affects the amount of surviving GNP and their crystallinity.

Commercial graphene nanoplatelets (N008-100-P-10, Angstron Materials Inc., U.S.) with thickness and x−y dimensions of 50−100 nm and 7 μm, respectively, were selected. A scanning electron micrograph of the pristine GNP is shown in Figure S1a of the supplementary information. The Fourier transform infrared-attenuated total reflectance (FTIR-ATR) spectrum of the GNP (Figure S1b) evidenced that nanoplatelets are functionalized, as different bands ascribed to the C=O carbonyl, C-O and -O-C epoxy chemical functional groups confirm. As it is seen in Figure S1c, these GNP are stable in air up to 550 ℃, while they show no significant weight loss up to 1000 ℃ in N_2.

Feedstock of each YAS matrix and GNP/YAS composites with increasing amounts of GNP (from 1 to 10 vol.%) were prepared for thermal spraying. The studied samples are presented in Table 2 and labelled as xYAS-y, were x is the initial amount of GNP in vol.% and y refers to L or H matrices. The process to obtain the sprayable granules of the formulated compositions from the corresponding powders is described in detail

elsewhere [15]. Briefly, stable aqueous suspensions were separately obtained for both the Y_2O_3-Al_2O_3-SiO_2 powders mixtures (Table 1) and the GNP. Batches of the YAS and GNP suspensions in the adequate proportion to get the targeted GNP percentages of Table 1 were then mixed by attrition milling for 30 min, and the final suspension was freeze-dried to avoid the segregation of the different constituents. From these homogeneous mixtures of GNP and Y_2O_3-Al_2O_3-SiO_2 powders, spherical granules of ~30 μm diameter were prepared by spray drying (SD). Batches of both plain YAS-L and YAS-H compositions were similarly processed to serve as reference materials. The different SD granules were flame sprayed over insulating cordierite ($2MgO \cdot 2Al_2O_3 \cdot 5SiO_2$) substrates (~ 15.5 x 5.5 x 3.0 mm^3) with an oxyacetylene torch (CastoDyn DS 8000, Castolin-Eutectic, Spain) using acetylene and oxygen pressures of 7.0×10^4 and 4.0×10^5 Pa, and gas flow rates of 4.0×10^{-4} and 5.4×10^{-4} $m^3 \cdot s^{-1}$ for each gas, respectively. Under these conditions, the adiabatic flame temperature was 3100 °C, well above the softening temperature of both glasses (~ 1000 °C). The distance of the torch to the substrate was 14 cm and a powder feed rate of 1.6×10^{-3} $kg \cdot s^{-1}$ was employed in all cases. The mean roughness of the cordierite substrates ($R_a = 9 \pm 1$ μm) facilitated proper adhesion between the substrate and the coatings. This substrate was selected because of its insulator character, reflected by an unmeasurable electrical conductivity with the current equipment. In fact, σ_m was below the experimental detection limit in the case of the YAS-L and YAS-H plain coatings on cordierite systems.

The amount of GNP enduring the harsh conditions of flame spraying was quantified for each composition by thermogravimetric (TGA) and differential thermal (DTA) analyses between room temperature and 1000 °C, using a heating rate of 10 °C·min⁻¹ in air (Perkin Elmer Pyris 1 TGA analyzer, USA). Figure S2 (supplementary information)

illustrates differences in the DTA/TGA analyses of the SD granules used as feedstock and the flame sprayed coatings for the case of the 10YAS-L composition, from which we can infer that weight loss from 600 to 950 ℃ is due to GNP combustion and it allows an accurate estimation of the GNP content in the coatings (Table 2). TGA for three different specimens of the same composition (10YAS-H) provides a standard deviation of 5%. As the accuracy of the balance is better than 0.02%, with a precision of 0.001 %, data error is associated to compositional variations in the specimens. In the 2.5YAS-L and 1YAS-L compositions, which showed very low weight losses, the carbon content was also measured by elemental analysis using a LECO-CS-200 apparatus (Table S1, supplementary information) giving alike figures as the TGA method.

Table 1. Composition of the two glasses used as matrix and temperatures for glass transition (T_g), first crystallization event (T_c) and melting (T_m) measured in bulk samples, which were prepared by melting and casting the corresponding powder compositions (from reference [21]). The densities (ρ) for both YAS compositions are also included.

Glass	Composition	T_g (℃)	T_c (℃)	T_m (℃)	ρ (g·cm^{-3})
YAS-L	$17.5Y_2O_3$-$29.5Al_2O_3$-$53.0SiO_2$	906	1118	1418	3.51
YAS-H	$33.0Y_2O_3$-$16.5Al_2O_3$-$50.5SiO_2$	929	1055	1525	3.91

The volume fraction of GNP within the coatings for each composition was estimated from the weight loss values and the corresponding densities (ρ) of GNP (2.20 g·cm^{-3}),

and YAS-L (3.51 g·cm^{-3}) and YAS-H (3.91 g·cm^{-3}) compositions. These latter densities were measured by immersion in water using bulk glass samples prepared by melting and casting each powder composition (data from a previous work [21]).

Table 2. Studied coating specimens for each matrix composition. Information includes the initial amount of GNP added, the specimen label, the weight loss determined by TGA, the final GNP volume content calculated from the weight loss and the density of the corresponding phases, and the thickness of the coatings.

Matrix	Initial GNP (vol.%)	Specimen label	Weight loss (%)	Final GNP (vol.%)	Thickness (μm)
YAS-L	0	0YAS-L	0	0	149 ± 14
	1	1YAS-L	0.1	0.16	129 ± 13
	2.5	2.5YAS-L	0.58	0. 92	121 ± 22
	5	5YAS-L	0.91	1.44	163 ± 10
	10	10YAS-L	2.30	3.62	120 ± 10
YAS-H	0	0YAS-H	0	0	143 ± 7
	5	5YAS-H	0.30	0.53	74 ± 7
	10	10YAS-H	0.68	1.20	109 ± 11

The GNP distribution within the coatings was plainly perceived by observing the coating polished cross sections and using a confocal μ-Raman spectroscopy (Alpha 300 WITech GmBH, Germany) with a 532 nm laser. Maps of 150 x 150 pixels were built with one spectrum per pixel using 60 ms of acquisition time, scanning an area of 45 x 45 μm^2 that is representative of the microstructural features in these coatings.

Electrical conductivity was determined by impedance spectroscopy and DC linear sweep voltammetry (Autolab potentiostat/galvanostat with frequency response analyser module PGSTAT 302N-FRA2, Eco Chemie, The Netherlands). The experimental setup consisted in a 4-probe configuration for more conductive samples and a 2-probe configuration for more resistive samples. The typical dimensions of the specimens (coating/substrate systems) were ~ 20.0 (length) x 4.5 (width) x 5.0 (thickness), in mm. In the 2-probe setup, Cu wires were attached with Ag electroconductive paste (Electrolube, ERSCP03B) to opposite edges (lengthwise) of the specimens, covering also the external cross-section surface of the coatings, in order to produce the current flow through the system and measure the voltage. In the 4-probe configuration, an additional pair of Cu wires was internally attached with Ag paste to measure the voltage and avoid any interference from the contact resistance in the experimental value. Note that the values of resistances associated to the higher-resistive coatings ($>10^3$ Ω) are several orders of magnitude higher than the electrical contact resistance because of the low GNP content and the low area-to-thickness ratio of the coating in the in-plane configuration. The resistance of the system was calculated from the slope of the V–I curve for DC measurements and from the total ohmic contribution in the impedance spectra. As cordierite is a dielectric material, the effective area (S) for the electrical transport corresponded to the coating cross section, that is $S \sim w \times t_c$, where w is the specimen width and t_c is the average coating thickness measured on scanning electron micrographs (table-top SEM TM1000 and FESEM S-4700, Hitachi, Japan) of coating cross sections, included in Table 2.

Additionally, the van der Pauw method [22] was used to measure DC sheet resistance (R_S) and Hall Effect to obtain carrier density (n) and mobility (μ) of conducting samples. A Keithley 2400 source-meter and a Keithley 2000 digital voltmeter managed by home-

made computer software were used to quantify I-V and V-H curves in a variable

magnetic field provided by a standard electromagnet (-0.8 T < H < 0.8 T).

UV-Vis optical reflectance measurements were performed using a Shimadzu SolidSpec-

3700 spectrophotometer in the range of 190 - 2600 nm. Solar absorptivity (α_{Sol}) is

evaluated from the experimentally obtained spectral reflectance data $R(\lambda)$ by:

$$\alpha_{Sol} = \frac{\int_{\lambda_1}^{\lambda_2}[1-R(\lambda)]A(\lambda)d\lambda}{\int_{\lambda_1}^{\lambda_2}A(\lambda)d\lambda} \qquad (2)$$

where $A(\lambda)$ is the ASTM AM1.5D solar spectral irradiance and integration limits $\lambda_1 =$

0.2 μm and $\lambda_2 = 2.6$ μm.

3. Results and discussion

All the coatings reached ~ 80% of the theoretical density, as estimated by the phase

composition and respective densities (Tables 1 and 2). As it can be seen in the SEM

images of the coatings cross section of the different coatings (Figure 1), the inter-splat

boundaries are better distinguished for the composite than for the plain coatings because

of the presence of dark features, which correspond mostly to nanoplatelets [15].
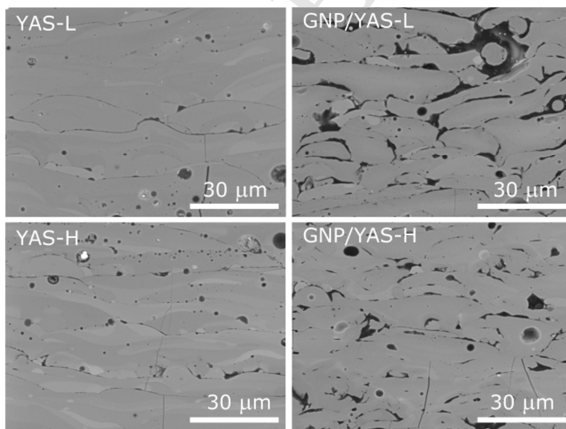
Figure 1. FESEM micrographs of the polished cross section of the YAS-L and YAS-H plain coatings and the composite coatings having 10 vol.% GNP in the original powder batches.

As proven in earlier works [15], the initial amount of GNP in the compositions decays after thermal spraying because the high temperatures (∼3100 ℃) and oxidative atmosphere involved induce its volatilization. Accordingly, the final GNP content in the coatings (see Figure 2 where a comparison for both matrices with equal GNP addition is presented) decreases around 70% for the YAS-L compositions, while the YAS-H attains reductions of ~ 90%. The smaller percentage of surviving nanoplatelets in YAS-H coatings can be attributed to both the higher melting temperature of this composition and the lower amount of energy absorbed from the flame for reacting and melting compared to YAS-L feedstock [16], which leaves higher amount of thermal energy available for the GNP burnt up.
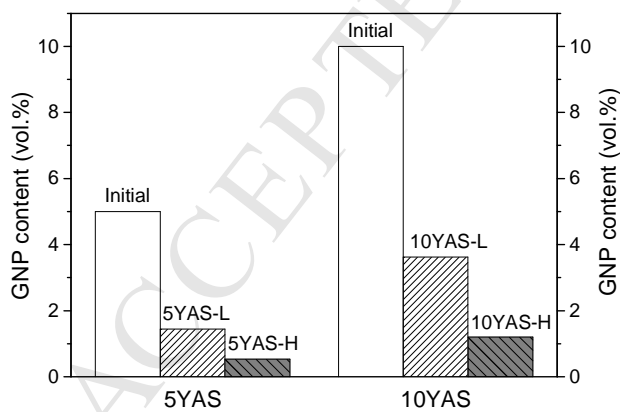

Figure 2. GNP content (in vol.%) in the initial powder composition and in the coatings (YAS-L and YAS-H) for 5YAS and 10YAS systems.

Figure 3 shows representative examples of the Raman study performed on the cross-section of the composite coatings (1YAS-L with the lowest content of 0.15 vol.% is not

shown as GNP was hardly detected by Raman). As it can see, the false-colors Raman images constructed by mapping the intensity of the G-band of GNP illustrate that nanoplatelets are clearly located at the inter-splat boundaries forming a network for GNP contents ≥ 1.20 vol.%. Conversely, GNP appears dispersed and isolated in those coatings with a content below 1.2 vol.%. The average Raman spectra of the graphene phase (Figure 4) show the characteristic D-, G- and 2D- bands of graphene-based materials [23] with a blue shift of the G-band (at 1591.5 and 1595.4 cm^{-1} for YAS-L and YAS-H matrices, respectively, in Table 3) as compared to that for the pristine GNP (1578.5 cm^{-1}). Similar blue-shift has been reported for bulk GNP/ceramic composites [13] and it is most probably associated to compressive strains induced by differences in the coefficients of thermal expansion (CTE) between the matrix and the GNP. CTE is 5 x 10^{-6} and 8 x 10^{-6} K^{-1} for YAS-L and YAS-H, respectively (measured on melted and casted bulk glass samples [21]) whereas the CTE of GNP for the plane of interest can be approximated to values reported for the graphite basal plane, i.e. varying from -1 to 1 x10^{-6} K^{-1} [24]. The effect of the ceramic substrate may also be important in rising residual stresses after cooling. On the other hand, the YAS matrix in both coatings (not shown here) showed two broad Raman bands, one centered at ∼ 950 cm^{-1}, assigned to the aluminosilicate glassy phase, and the other band around 400 cm^{-1}, associated to nucleation and crystallization processes that is comparatively more intense for YAS-H composition [15,16].

The intensity ratio –in area- between D- and G-peaks (I_D/I_G) for the average Raman spectrum of the composite coatings is higher (∼ 0.35 for YAS-L and > 0.65 for YAS-H based coatings) than that for the pristine GNP (0.11). Although a higher weight of the defective GNP edges in the Raman signal when analyzing the coating cross-section could affect I_D/I_G, the oxidation of the GNP during the thermal spraying process may be

also significant. In fact, as it has been previously proved by DTA/TGA [16], YAS-H absorbs a lower amount of energy for reacting and melting compared to YAS-L, which may explain both the smaller percentage of surviving nanoplatelets in YAS-H coatings (Figure 2) and their higher I_D/I_G, as the amount of thermal energy available for the GNP burnt up would be comparatively higher.
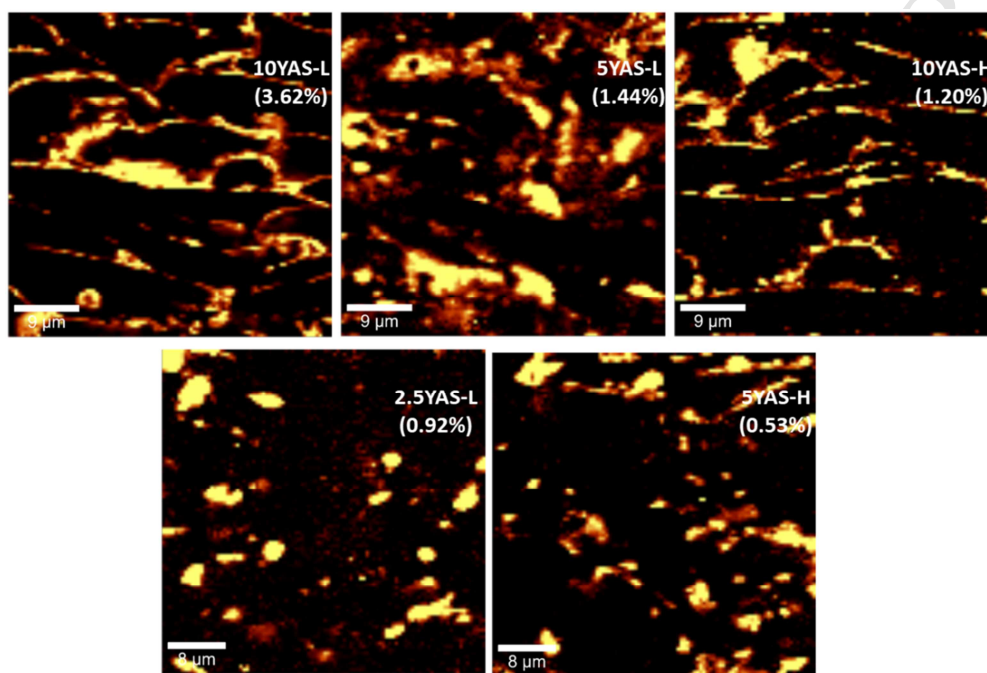

Figure 3. False colored images built by filtering the intensity of the G-band of GNP for Raman maps acquired on the cross sections (areas of 45 x 45 μm^2) of the composite coatings. Final GNP content (in vol.%) within the coating is included between parentheses.
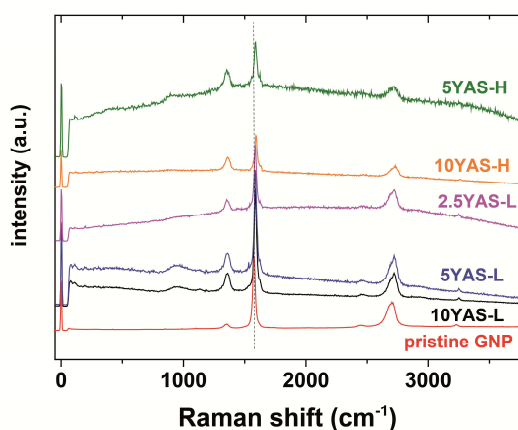
Figure 4. Average Raman spectra of the pristine GNP and composite coatings in the maps of Figure 3.

Table 3. Position of the D-, G- and 2D- bands of the GNP, and intensity ratio between D- and G-peaks (I_D/I_G), for the average Raman spectra of the GNP in the composite coatings.

Sample	Position (cm^{-1})			I_D/I_G
	D	G	2D	
10 YAS-L	1361.0	1585.9	2720.9	0.34
5YAS-L	1361.0	1585.9	2720.9	0.40
2.5 YAS-L	1352.7	1585.9	2714.0	0.35
10YAS-H	1361.5	1591.4	2730.4	0.65
5YAS-H	1357.0	1589.9	2717.4	0.77
Pristine GNP	1352.6	1578.5	2711.0	0.11

Figure 5a shows the dependence of the electrical conductivity of all the coatings with the GNP volume fraction. The electrical behavior of the coatings can clearly be described by percolation models. Fitting of the experimental data to the simplest

percolation model of Eq. (2) gives a percolation threshold of $V_{h,c} = 0.0118$ with a value of $t = 2$, and $\sigma_{h(GNP)} = 10^5$ S·m^{-1}. On the other hand, the general effective media (GEM) equation can also be used to fit experimental data. This equation is commonly applied to insulator/conductor binary mixtures and has the advantage over conventional percolation models that it allows the analysis of data close to the percolation threshold [25]. According to this model:

$$\frac{(1-V_h)(\sigma_l^{1/t}-\sigma_m^{1/t})}{\sigma_l^{1/t}+A\sigma_m^{1/t}} + \frac{V_h(\sigma_h^{1/t}-\sigma_m^{1/t})}{\sigma_h^{1/t}+A\sigma_m^{1/t}} = 0 \;, \qquad\qquad A = \frac{(1-V_{h,c})}{V_{h,c}} \qquad\qquad (3)$$

where σ_m is the electrical conductivity of the binary mixture, σ_l is the conductivity of the insulating matrix and σ_h is the conductivity of the conducting particles (GNP). The fitting of the experimental data to this equation, assuming $\sigma_l = 10^{-11}$ S·m^{-1} for the insulator YAS matrix, is also included in Figure 5a (dashed line) and provides fitting parameters equal to those deduced from the simple percolation model. The t exponent in Eqs. (1) and (3) depends on the connectivity mode, i.e. the shape and orientation of the conducting phase; the widely accepted theoretical value for a three-dimensional (3D) network is 2 and, thus, a 3D connectivity of the GNP is inferred for these composite coatings. This universal value was also observed in anisotropic GNP/Si$_3$N$_4$ materials when tested in the direction perpendicular to the SPS axis, equivalent to the present GNP orientation regarding the electrical conductivity tests, while a critical exponent close to 1 was observed when tested in the parallel direction [8].

The estimated upper limit for σ_h of the GNP fillers (10^5 S·m^{-1}) is lower than the value measured along the ab-plane of single-crystal graphite (1.7 x 10^6 S·m^{-1} [26]) and also below values reported for σ_h fitting by the GEM equation in the case of GNP highly oriented bulk Si$_3$N$_4$/GNP composites (6.25 x 10^6 S·m^{-1}) [8] or for expandable graphite monoliths (1.0 x 10^6 S·m^{-1}) [27]. On the other hand, σ_h values (8.3 x 10^4 S·m^{-1}) below

the value deduced here for the present coatings were obtained for GO fillers by fitting the conductivity data to the GEM equation for GO/polystyrene composites [28]. In fact, the electrical conductivity for thermally reduced GO (rGO) films has been shown to depend on the sp^2 carbon fraction that gradually rises with the loss of oxygen, reaching a maximum value of ~ 5.5 x 10^4 S·m^{-1} for fully reduced GO with a residual oxygen content of ~8 at.% [29]. Therefore, the low σ_h for the present graphene nanofillers could be then attributed to two main reasons: i) a contact resistance between filler particles which is included in the resistivity of the filler in the effective media model, and ii) some oxidation of the nanoplatelets during the thermal spraying process, which is supported by the larger I_D/I_G ratio determined for GNP in the coatings (0.35-0.77 in Table 3); in fact, this ratio is even above that reported for rGO/Si_3N_4 composites (0.3), where GO fillers were in-situ reduced during the composite densification in the spark plasma sintering furnace [8]. Moreover, the high porosity (20%) associated to the current coatings is expected to decrease the experimental conductivity due to the enlargement of the effective path of conduction compared to the experimentally measured distances.

The obtained critical GNP percolation volume fraction ($V_{h,c}$ = 0.0118) is within the lowest reported up to now for graphene/ceramic composites (Figure 5b), which show critical volume filler contents for percolation ranging between 0.38 and 2.0 % for rGO containing composites [7-9] and from 2.0 up to 9.0 for composites with thicker GNP [8,10,30,31]. Therefore, this limit appears obviously related to the distribution and dispersion of the fillers. For the present GNP/YAS coatings, the percolation limit is within the range of values reported for highly exfoliated rGO but it is below than those reported for ceramic composites with well dispersed GNP of similar thickness and, therefore, it should be related to the reticulated GNP pattern linked to thermal spraying

processes. In the case of highly dispersed rGO/fused silica bulk composites [9], a percolation threshold of ∼ 0.58 vol.% has been reported (presently estimated from reported data of 0.58 wt. % and considering that density of fused silica matrix is close to that of rGO), showing a dependence of the electrical conductivity with the graphene filler content comparable to the present GNP/YAS coatings as well. These rGO/fused silica composites -obtained by SPS from GO/amino-modified silica fused composite particles- presented a microstructure of dispersed rGO sheets located at the boundaries between glassy particles that certainly reminds that of the present coatings. Furthermore, present results also agree with those reported on epoxy and polyurethane composite films of similar thicknesses (~100-200 μm) containing oriented graphite flakes (x-y dimensions = 10 μm and thickness of 100 nm), where similar values for critical volume (0.8-1.2 %) and t exponent (t= 2.5 - 2) were calculated using the percolation model [17-19].

Additionally, sheet resistance, carrier density and mobility of 10YAS-L, 5YAS-L and 10YAS-H conducting coatings were measured by the van der Pauw method using a DC current source. The obtained conductivity values are in perfect agreement with those obtained by AC impedance spectroscopy and DC linear sweep voltammetry (plotted in Figure 5a) and, on the other hand, Hall Effect shows n-type conduction. This result is in agreement with experimental and theoretical studies of graphene supported on Si/SiO_2 substrates [32] which indicates that electronic surface states of SiO_2 donate electrons to graphene and hence the n-type behavior is intrinsic to the SiO_2/graphene interface.
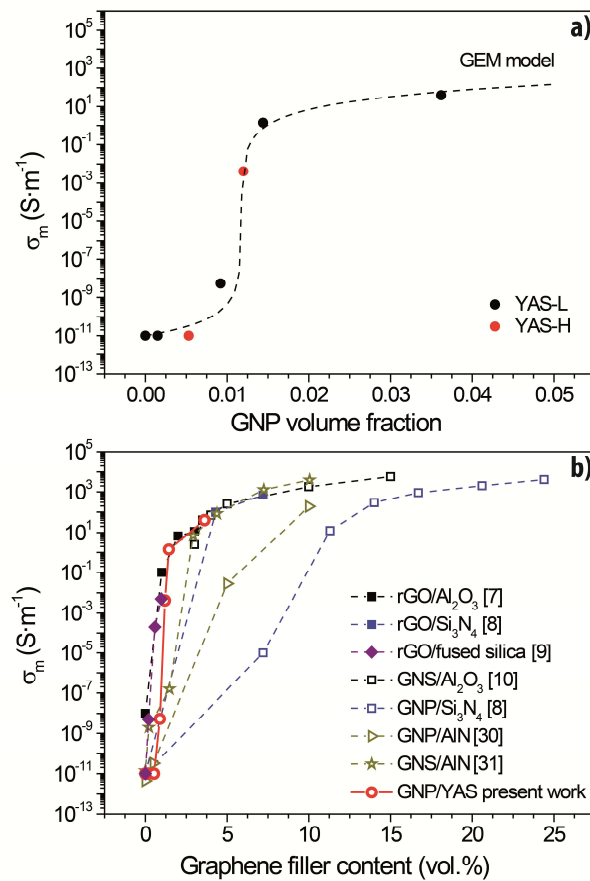
Figure 5. (a) Electrical conductivity (σ_m) as a function of the GNP volume fraction for the GNP/YAS coatings: symbols correspond to the experimental data and the dashed lines show the best fitting for the GEM equation (3). (b) Comparison of the present electrical conductivity values with data from literature for different insulator ceramics plotted as a function of the graphene filler content in vol.%. Dashed lines in this case are only for eye guide, and empty and full symbols correspond to GNP and rGO fillers, respectively. GNS probably refers to GNP, although the cited work does not give a clear indication. Replotted from reference [6].

The values for carrier density and mobility are collected in Table 4 and plotted in Figure 6 together with other ones reported in the literature for bulk graphene/ceramic

composites. Figure 6 shows rising trends with the graphene content for both the carrier density and mobility, although differences observed depending on the type of graphene filler deserve a comment. In fact, considering all the data, a consistent linear trend is perceived for mobility, which is explained by an increasing connectivity between the graphene flakes and points toward a minor effect of the ceramic matrix. Moreover, the dominant role of thermally activated tunneling for filler contents above but close to the percolation threshold has been demonstrated in the case of polymer composite films with graphite flakes that showed electrical behavior similar to the present coatings [19].

The trend observed for the carrier density in Figure 6 is not straightforward, as it exhibits a linear dependence with graphene content for the samples containing GNP (GNP/YAS and GNP/Si_3N_4 systems) but deviates for the rGO/Si_3N_4 system showing a significantly higher value, despite this material has filler content close to the 10YAS-L system. This greater carrier density points to a higher doping in rGO than in GNP systems [33], which may be affected by the interaction with the matrix. Actually, the GNP/Si_3N_4 and rGO/Si_3N_4 interfaces have been proved to be quite different [33,34], showing an amorphous grain boundary layer of ca. 2 nm thick for the GNP but only a thin graphene layer with the typical defective zones at the edges of the rGO sheets, residues from the reduction process, at rGO/Si_3N_4 interfaces. Furthermore, nano-clusters (2–5 nm) of disordered/defective zones on the graphene plane separated by less than 5 nm have been detected for rGO/Si_3N_4 materials [33], which would explain the slightly lower mobility observed in this system when compared to the 10YAS-L sample.

Table 4. Sheet resistance (R_s), carrier density (n) and mobility (μ) for the conducting coatings of this work and for bulk graphene/ceramic composites in the literature.

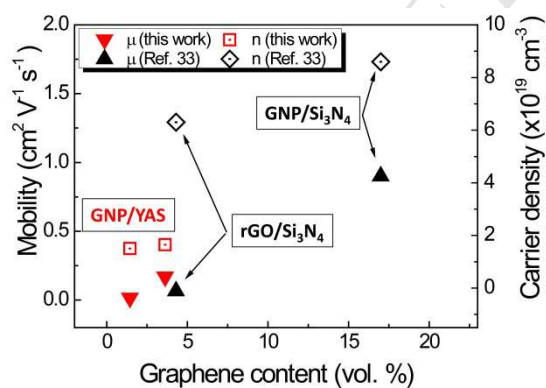| Material	Filler (vol.%)	R_S $\Omega \cdot sq^{-1}$	n (x $10^{19}cm^{-3}$)	μ ($cm^2 \cdot V^{-1} \cdot s^{-1}$)	Source
10YAS-L	3.62	1.8×10^2	1.65 ± 0.15	0.17 ± 0.3	
5YAS-L	1.44	2.7×10^3	1.5 ± 0.5	0.016 ± 0.05	present work
10YAS-H	1.20	1.2×10^5	-----	-----	
GNP/Si$_3$N$_4$	17		6.3	0.9	[33]
rGO/Si$_3$N$_4$	4.3		8.6	0.065	

Figure 6. Mobility (μ) and carrier density (n) vs. the graphene filler content for conducting GNP/YAS coatings and other data from literature for bulk graphene/Si$_3$N$_4$ composites [33].

The microstructure of the present composite coatings would perfectly correspond to the so-call segregated systems for cellular structures, which is schematically illustrated in the insert of Figure 7, where a fine conducting phase forms a percolation path on the surface of the coarse insulating particles. There are several models [35-37] that predict, for this type of systems, a strong influence of the particle size ratio (R_p/R_m, where R_p is the radius of the primary phase particle and R_m is the radius of the disperse phase particle) on the continuity of aggregates. According to Kusy [36], the critical volume fraction of dispersed material required for continuity can be expressed as

$$V_{h,c} = [1+\alpha\cdot(R_p/R_m)]^{-1} \tag{4}$$

where α is a parameter related to the geometry of the system. This equation is represented in Figure 7 for cubic lattices for the ideal case (black line) in which the dispersed phase is totally efficient and α in Eq. (4) is 1.51 and the practical situation (red line) where the dispersed phase has an equal propensity to penetrate the surface and to fill the interstices of the primary phase ($\alpha = 0.76$); as it can be seen, a percolation limit in the range of 0.02-0.04 is estimated for a segregated system with $R_p/R_m = 30$ [36]. For the present coatings the radius of primary phase particle is the splat size (radius of ∼15 μm); whereas R_m would be the GNP thickness (50-100 nm). Therefore, R_p/R_m is ∼150, with $V_{h,c}$ approaching to 0.01, which is close to the experimental percolation threshold of 0.0118.
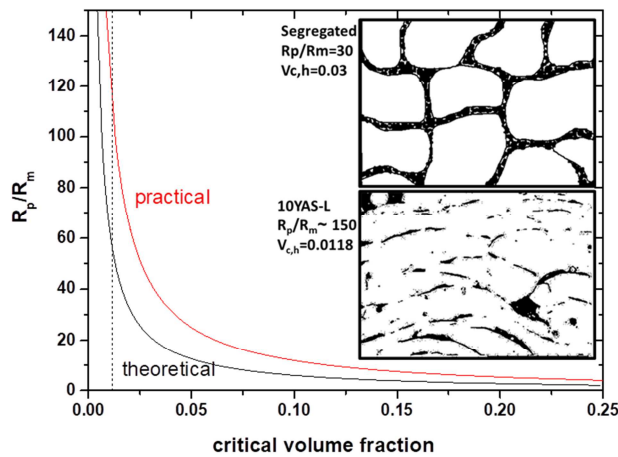
Figure 7. Kusy's simulation curves for the relationship between R_p/R_m and the critical volume fraction in a cubic lattice: in black the ideal situation in which the dispersed phase is totally efficient ($\alpha = 1.51$ in Eq. (4)) and, in red, the practical case where the dispersed phase has an equal propensity to penetrate the surface and to fill the interstices of the primary phase ($\alpha = 0.76$). The dashed line corresponds to the critical volume fraction of the GNP/YAS coatings. The insert shows a basic microstructure model of a segregated cellular system (insulator in white and fine conducting phase in black) that shows a percolation threshold of 0.03 for a radius ratio of about 30 (from reference [35] and a black and white image of the present 10YAS-L composite coating where the GNP (in black) forms a percolation path on the surface of the insulating glass particles (in white).
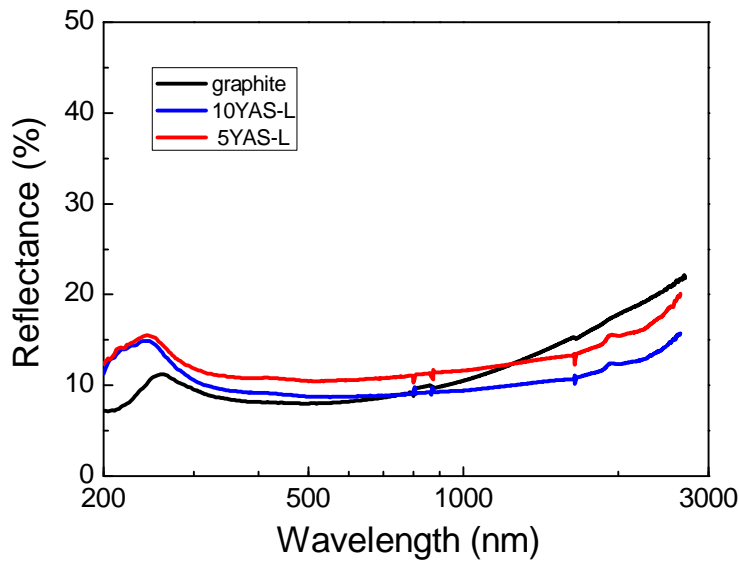
Figure 8. Optical reflectance of 5YAS-L and 10YAS-L coatings. Measurement of commercial graphite specimen (Carbone Lorraine, grade 2230) is included for comparison.

As seen in Figure 8, optical reflectivity of 5YAS-L and 10YAS-L coatings is similar to that of graphite but slight differences may be observed at wavelengths below 300 nm where both coatings present higher reflectivity than graphite. The solar absorptivity of the coating surface, i.e. its effectiveness in absorbing solar radiant energy, is also very similar for the three materials in the selected spectral interval: 90.0, 90.6 and 88.6 % for graphite, 10YAS-L and 5YAS-L, respectively, which makes these coatings suitable for thermal protection systems (TPS) in aerospace applications because of two complementary performances: collector of thermal energy from the Sun and its high thermal load resistance [16] essential for protection against high reentry temperatures. These coatings could be also interesting as photothermal detectors and solar absorbers for applications such as solar steam generation and water desalination [39,40]. It should also be considered that these coatings can be sprayed on uneven substrates (rough, patterned or porous) and even non-flat surfaces, which also increase its attractiveness.

4. **Conclusions**

Thick graphene/glass composite coatings containing evenly spaced graphene nanofillers with a quite remarkable low percolation limit (1.18 vol.%) for electrical conduction have been achieved using the cost-effective thermal spraying method. The electrical behavior of these GNP/YAS glass composite coatings is undoubtedly related to the microstructure generated by the spraying process. In this way, the percolation limit is determined by the ratio between the splat size and the GNP thickness and could be reasonably controlled. The estimated upper limit for the electrical conductivity of GNP is relatively low (10^5 S·m^{-1}) due to both the GNP/GNP contact resistance that is included in the resistivity of the filler in GEM model and some oxidation of the GNP during the thermal spraying. Hall Effect shows the n-type behavior typical of the silica/graphene interface, and carrier density and mobility of the same order of those reported for bulk ceramic composites containing graphene type fillers. These results jointly with the very high solar absorptivity of the coating surface broaden the applications of these systems, as for instance in electromagnetic interference shielding or as photothermal detectors and solar absorbers for solar steam generation and water desalination.

Acknowledgements

References

[1] Zhu Y, Murali S, Cai W, Li X, Suk JW, Potts JR, Ruoff RS. Graphene and graphene oxide: synthesis, properties, and applications. Adv Mater 2010; 22 (35):3906–3924.

[2] Soldano C, Mahmood A, Dujardin E. Production, properties and potential of graphene. Carbon 2010; 48 (8):2127–2150.

[3] Novoselov KS, Fal VI, Colombo L, Gellert PR, Schwab MG, Kim K. A roadmap for graphene. Nature 2012; 490 (7419):192-200.

[4] Ferrari AC, Bonaccorso F, Fal'ko V, Novoselov KS, Roche S, Bøggild P, et al. Science and technology roadmap for graphene related two-dimensional crystals, and hybrid systems. Nanoscale 2015; 7(11):4587-5062.

[5] Young RJ, Kinloch IA, Gong L, Novoselov KS. The mechanics of graphene nanocomposites: A review. Compos Sci Technol 2012; 72(12):1459–1476.

[6] Miranzo P, Belmonte M, Osendi MI. From bulk to cellular structures: A review on ceramic/graphene filler composites. J Eur Ceram Soc 2017; 37(12):3649-3672.

[7] Centeno A, Rocha VG, Alonso B, Fernandez A, Gutierrez-Gonzalez CF, Torrecillas R, et al. Graphene for tough and electroconductive alumina ceramics. J Eur Ceram Soc 2013; 33 (15–16):3201-3210.

[8] Ramirez C, Vega-Diaz SM, Morelos-Gomez A, Figueiredo FM, Terrones M, Osendi MI, et al. Synthesis of conducting graphene/Si_3N_4 composites by spark plasma sintering. Carbon 2013; 57:425-432

[9] Chen B, Liu X, Zhao X, Wang L, Jiang W, Li J. Preparation and properties of reduced graphene oxide/fused silica composites. Carbon 2014; 77: 66-75

[10] Fan YC, Jiang W, Kawasaki A. Highly conductive few-layer graphene/Al_2O_3 nanocomposites with tunable charge carrier type. Adv Func Mater 2012; 22 (18):3882–3889.

[11] Ramírez C, Figueiredo FM, Miranzo P, Poza P, Osendi MI. Graphene nanoplatelet/silicon nitride composites with high electrical conductivity. Carbon 2012; 50: 3607-3615.

[12] Ramirez C, Osendi MI, Miranzo P, Belmonte M, Figueiredo FM, Castro-Beltrán A, Terrones M. Graphene nanoribbon ceramic composites, Carbon 2015; 90:207–214.

[13] Roman-Manso B, Domingues E, Figueiredo FM, Belmonte M, Miranzo P. Enhanced electrical conductivity of silicon carbide ceramics by addition of graphene nanoplatelets, J Eur Ceram Soc 2015; 35 (10):2723–2731.

[14] Belmonte M, Nistal A, Cruz-Silva R, Morelos-Gómez A, Terrones M, Miranzo P, et al. Directional electrical transport in tough multifunctional layered ceramic/graphene composites. Adv Electron Mater 2015; 1(9):1500132.

[15] Garcia E, Nistal A, Khalifa A, Essa Y, Martin de la Escalera F, Osendi MI, et al. Highly electrically conducting glass-graphene nanoplatelets hybrid coatings, ACS Appl Mater Interfaces 2015; 7 (32):17656–17662.

[16] Garcia E, Nistal A, Osendi MI, Miranzo P. Superior performance of ablative glass coatings containing graphene nanosheets, J Am Ceram Soc 2016; 36 (16):3987–3993.

[17] Celzard A, McRae E, Mareche JF, Furdin G, Dufort M, Deleuze C. Composites based on micron-sized exfoliated graphite particles: electrical conduction, critical exponents and anisotropy. J Phys Chem Solids 1996; 57 (6-8): 715-718.

[18] Celzard A, McRae E, Marêché JF, Furdin G, Sundqvist B. Conduction mechanisms in some graphite–polymer composites: effects of temperature and hydrostatic pressure. J Appl Phys 1998; 83 (3): 1410-1419.

[19] Celzard A, McRae E, Furdin G, Mareche JF. Conduction mechanisms in some graphite-polymer composites: the effect of a direct-current electric field. J Phys Cond Matter 1997; 9 (10): 2225.

[20] Celzard A, McRae E, Deleuze C, Dufort M, Furdin G, Marêché JF. Critical concentration in percolating systems containing a high-aspect-ratio filler. Phys Rev B 1996; 53 (10): 6209.

[21] Marraco-Borderas C, Nistal A, García E, Sainz MA, Martin de la Escalera F, Essa Y, et al. Adhesion of Y_2O_3-Al_2O_3-SiO_2 coatings to typical aerospace substrates. Bol Soc Esp Ceram V 2016; 55 (4):127–35.

[22] Van der Pauw LJ. A method of measuring specific resistivity and Hall effect of discs of arbitrary shape. Philips Res Rep 1958; 13: 1-9.

[23] Ferrari AC, Meyer JC, Scardaci V, Casiraghi C, Lazzeri M, Mauri F, et al. Raman spectrum of graphene and graphene layers. Phys. Rev. Lett. 2006; 97: 187401-187404.

[24] Tsang DKL, Marsden BJ, Fok SL, Hall G. Graphite thermal expansion relationship for different temperature ranges. Carbon, 2005; 43 (14): 2902-2906.

[25] McLachlan DS, Blaszklewicz M, Newnham RE. Electrical resistivity of composites. J Am Ceram Soc 1990; 73(8):2187-2203.

[26] Edman L, Sundqvist B, McRae E, Litvin-Staszewska E. Electrical resistivity of single-crystal graphite under pressure: an anisotropic three-dimensional semimetal.

[27] Celzard A, Mareche JF, Furdin G, Puricelli S. Electrical conductivity of anisotropic expanded graphite-based monoliths. J Phys D: Appl Phys 2000; 33:3094–101.

[28] Stankovich S, Dikin DA, Dommett GH, Kohlhaas KM, Zimney EJ, Stach EA, et al. Graphene-based composite materials. Nature Lett. 2006; 442:282–6.

[29] Mattevi C, Eda G, Agnoli S, Miller S, Mkhoyan KA, Celik O, et al. Evolution of electrical, chemical, and structural properties of transparent and conducting chemically derived graphene thin films. Adv Func Mater 2009, 19(16):2577-2583.

[30] Simsek ING, Nistal A, García E, Pérez-Coll D, Miranzo P, Osendi MI. The effect of graphene nanoplatelets on the thermal and electrical properties of aluminum nitride ceramics. J Eur Ceram Soc 2017; 37:3721-3729.

[31] Yun C, Feng YB, Qiu T, Yang J, Li XY, Yu L. Mechanical, electrical, and thermal properties of graphene nanosheet/aluminum nitride composites. Ceram Inter 2015; 41 (7):8643-8649.

[32] Romero HE, Shen N, Joshi P, Gutierrez HR, Tadigadapa SA, Sofo JO, et al. n-type behavior of graphene supported on Si/SiO_2 substrates. ACS Nano 2008; 2 (10): 2037-2044.

[33] Ramirez C, Leborán V, Rivadulla F, Miranzo P, Osendi MI. Thermopower and hall effect in silicon nitride composites containing thermally reduced graphene and pure graphene nanosheets. Ceram Inter 2016; 42 (9): 11341-11347.

[34] Ramirez C, Miranzo P, Belmonte M, Osendi MI, Poza P, Vega-Diaz SM, et al. Extraordinary toughening enhancement and flexural strength in Si_3N_4 composites using graphene sheets. J Eur Ceram Soc 2014; 34 (2): 161-169.

[35] McLachlan DS, Sauti G. The AC and DC conductivity of nanocomposites. Journal of Nanomaterials 2007. Article ID 30389, 9 pages. doi:10.1155/2007/30389.

[36] Kusy RP. Influence of particle size ratio on the continuity of aggregates. J Appl Phys 1977; 48(12):5301-5305.

[37] Garboczi EJ, Snyder KA, Douglas JF, Thorpe MF. Geometrical percolation threshold of overlapping ellipsoids. Phys Rev E 1995; 52(1):819.

[38] Vionnet-Menot S, Grimaldi C, Maeder T, Strässler S, Ryser P. Tunneling-percolation origin of nonuniversality: theory and experiments. Phys Rev B 2005; 71(6):064201.

[39] Li X, Xu W, Tang M, Zhou L, Zhu B, Zhu S, Zhu J. Graphene oxide-based efficient and scalable solar desalination under one sun with a confined 2D water path. PNAS 2016; 113(49): 13953-13958.

[40] Song H, Liu Y, Liu Z, Singer MH, Li C, Cheney AR, et al. Cold Vapor Generation beyond the Input Solar Energy Limit. Adv. Sci. 2018: 1800222.